

Pfungst and Clever Hans: Identifying the unintended cues in a widely used Alzheimer’s disease MRI dataset using explainable deep learning

Christian Tinauer¹[0000–0003–4355–3898], Maximilian Sackl¹[0000–0002–1927–7953], Rudolf Stollberger^{2,3}[0000–0002–4969–3878], Stefan Ropele^{1,3}[0000–0002–5559–768X], and Christian Langkammer^{1,3}[0000–0002–7097–9707],
for the Alzheimer’s Disease Neuroimaging Initiative*

¹ Department of Neurology, Medical University of Graz, 8036 Graz, Austria
{christian.tinauer,christian.langkammer}@medunigraz.at
<https://neuroimaging.at>

² Institute of Biomedical Imaging, Graz University of Technology, 8010 Graz, Austria

³ BioTechMed-Graz, 8010 Graz, Austria

Abstract.

Backgrounds. Deep neural networks have demonstrated high accuracy in classifying Alzheimer’s disease (AD). This study aims to enlighten the underlying black-box nature and reveal individual contributions of T1-weighted (T1w) gray-white matter texture, volumetric information and preprocessing on classification performance.

Methods. We utilized T1w MRI data from the Alzheimer’s Disease Neuroimaging Initiative to distinguish matched AD patients (990 MRIs) from healthy controls (990 MRIs). Preprocessing included skull stripping and binarization at varying thresholds to systematically eliminate texture information. A deep neural network was trained on these configurations, and the model performance was compared using McNemar tests with discrete Bonferroni-Holm correction. Layer-wise Relevance Propagation (LRP) and structural similarity metrics between heatmaps were applied to analyze learned features.

Results. Classification performance metrics (accuracy, sensitivity, and specificity) were comparable across all configurations, indicating a negligible influence of T1w gray- and white signal texture. Models trained on binarized images demonstrated similar feature performance and relevance distributions, with volumetric features such as atrophy and skull-stripping features emerging as primary contributors.

Conclusions. We revealed a previously undiscovered Clever Hans effect in a widely used AD MRI dataset. Deep neural networks classification predominantly rely on volumetric features, while eliminating gray-white matter T1w texture did not decrease the performance. This study clearly demonstrates an overestimation of the importance of gray-white matter contrasts, at least for widely used structural T1w images, and highlights potential misinterpretation of performance metrics.

*Data used in preparation of this article were obtained from the Alzheimer’s Disease Neuroimaging Initiative (ADNI) database (<https://adni.loni.usc.edu>). As such, the investigators within the ADNI contributed to the design and implementation of ADNI and/or provided data but did not participate in analysis or writing of this report. A complete listing of ADNI investigators can be found at: https://adni.loni.usc.edu/wp-content/uploads/how_to_apply/ADNI_Acknowledgement_List.pdf

Keywords: Clever Hans effect · Alzheimer’s disease · MRI · deep learning · heatmapping

1 Introduction

Alzheimer’s disease (AD) is the most common form of dementia, accounting for 60-70% of cases [26] and with over 55 million people worldwide living with some form of dementia, it poses a substantial burden on healthcare systems, caregivers, and families [1]. However, in vivo diagnosis remains challenging due to the overlap of clinical symptoms with other conditions, resulting in relatively low diagnostic accuracy (71-87% sensitivity and 44-71% specificity) [3].

In addition to clinical and neuropsychological assessments, medical imaging is employed to improve diagnostic accuracy. Positron emission tomography (PET) imaging with amyloid and tau protein ligands, combined with magnetic resonance imaging (MRI), has become a valuable tool in AD diagnosis [11]. Yet, AD is characterized by a prolonged prodromal and asymptomatic inflammatory phase, during which PET imaging is unsuitable for predicting disease onset in healthy populations. Since pathological changes in AD begin decades before clinical symptoms appear, MRI holds promise for identifying early biomarkers in a broad population. Currently, brain volumetry [29], particularly hippocampal atrophy [13], is widely used as an imaging marker for differential diagnosis and in interventional studies.

In recent years, convolutional neural networks (CNNs) have emerged as the state-of-the-art method for AD classification using structural T1-weighted (T1w) MRI scans [36]. These networks learn image features directly during the training process, eliminating the need for manual feature selection. Despite their advantages, CNN models and the features they extract are often difficult for humans to interpret, earning them the reputation of being “black boxes” [8].

To address this issue, interpretability methods such as heatmapping have been introduced [28]. One notable technique is Layer-wise Relevance Propagation (LRP) [2], which highlights the features in input images that contribute most significantly to the model’s classification decisions. The importance of interpretability is underscored by examples like described in [19], where a deep neural network erroneously identified horses based on secondary photo watermarks rather than the animals themselves. This type of bias, known as the *Clever Hans effect*, illustrates how unintended cues can influence model predictions [35]. The term originates from the early 20th century, when a horse named Clever Hans was believed to perform arithmetic but was later discovered by Mr. Pfungst to rely on subtle cues from the test setup and interviewer, rather than actual calculation ability [25].

Previous research on interpretable CNNs for AD classification has demonstrated that preprocessing steps can significantly impact model performance and the features extracted during training [33]. We hypothesize that a commonly applied preprocessing step -skull-stripping- may introduce unintended features, leading to the neglect of more relevant AD-specific changes, such as structural changes and gray-white matter contrast variations [7].

In this study, we combined deep learning and heatmapping explainability techniques to evaluate the performance and learned features of CNNs trained on different input configurations. Specifically, we trained identical CNN architectures on full T1w images from the Alzheimer’s Disease Neuroimaging Initiative (ADNI) dataset, their skull-stripped counterparts, and three differently binarized versions

of these two preprocessing approaches, creating a total of eight model configurations. We analyzed performance metrics for significant differences and used structural image similarities of the resulting heatmaps to investigate whether preprocessing introduces unintended cues.

2 Materials and Methods

2.1 Imaging Data

Using MR image metadata from the ADNI database, we created a subset of images with clinically available and consistent properties. The final search criteria were: Phase = ADNI 2, Acquisition Plane = SAGITTAL, Field Strength = 3.0 Tesla, Pixel Spacing XY = [1.0 mm, 1.1 mm], Slice Thickness = 1.2 mm, and Weighting = T1. These criteria resulted in 1,042 images for the AD group and 2,227 images for the normal control (NC) group. This ensured that patients and controls were scanned using a consistent MRI protocol at 3 Tesla across multiple scanner vendors and sites. Supplementary Table 4 and Supplementary Table 5 in Supplemental Material 1 summarize the distribution of images across sites, vendors, imaging protocols and research groups.

2.2 Research Groups

We retrospectively selected 990 MR images from 159 patients with AD and 990 MR images from 201 propensity-logit-matched (covariates: age, sex) NC from the preselected image data subset [18]. Table 1 shows the demographics of the selection. Data were split into training, validation, and test sets (ratio 70:15:15), ensuring that all scans from a given individual were included in the same set. To maintain consistent class distribution, the final sets were created by combining data from both cohorts.

Table 1: Summary of subject demographics at baseline for ADNI. Note. Values are presented as mean \pm SD [range]. M: male, F: female, MMSE: mini-mental state examination, CDR: global clinical dementia rating, n/a: no value available.

	Subjects	Images	Age	Gender	MMSE	CDR
NC	201	990	75.1 \pm 7.1 [56.3, 95.8]	102 M/99 F	28.9 \pm 1.2 [24.0, 30.0] n/a: 16	0.0: 171; 0.5: 13; n/a: 17
AD	159	990	75.3 \pm 7.9 [55.7, 91.5]	91 M/68 F	22.0 \pm 3.8 [4.0, 30.0] n/a: 48	0.5: 35; 1.0: 67; 2.0: 9; n/a: 48

2.3 Preprocessing

Raw T1w images were reoriented to standard space using FSL-REORIENT2STD [16], cropped to a 160 \times 240 \times 256 matrix size, bias field corrected using N4 [34], and non-linearly registered to the

MNI152 template via FSL-FNIRT [16]. Intensity values were normalized to the white matter peak of the brain tissue histogram (196 bins). The outputs of this preprocessing pipeline are referred to as “aligned” images. Individual brain masks were generated in native image space using SIENAX from FSL [30] and warped to the aligned images to create the “skull-stripped” images. Binary masks preserving shape information were derived using manually selected thresholds of 13.75%, 27.5%, and 41.25% of the white matter peak of the brain tissue histogram and the aligned images. These binary masks were also combined with skull-stripped preprocessing, resulting in eight total setups, as illustrated in Figure 1.

2.4 Standard classification network

We utilized a conventional 3D subject-level classifier network as described in [36]. However, because the number of trainable parameters (42 million) relative to the dataset size (1980 images) is high, the network is prone to overfitting. To address this, we reduced the number and size of the convolutional and fully connected layers until the network no longer overfit the training data and the validation accuracy ceased to improve. Batch normalization layers did not influence the network’s performance and were therefore omitted. Additionally, we replaced max pooling layers with convolutional layers using striding, as tested in [31]. This modification improves the interpretability of the network [24]. Dropout was not applied in the network. To further enhance interpretability, all biases in the classifier were constrained to be non-positive, which helped sparsify the network activations [24]. The final 3D classifier network, as shown in Figure 2, consists of a single convolutional layer (kernel size: $3 \times 3 \times 3$, 8 channels) combined with a down-convolutional layer (kernel size: $3 \times 3 \times 3$, 8 channels, striding: 2) as its primary building block. The network stacks four of these main building blocks, followed by two fully connected layers (with 16 and 2 units, respectively), resulting in a total of 0.3 million trainable parameters. Each layer is followed by a Rectified Linear Unit activation function, except for the output layer, which employs a Softmax activation.

2.5 Training

Models were trained on aligned images, skull-stripped images, and their binarized counterparts. Training was performed using the Adam optimizer [17] for 30 epochs with a batch size of 20 using three independent network weights initializations [5] minimizing the binary cross entropy loss. Each data sampling was trained with all three initializations.

2.6 Heatmapping and relevance-weighted heatmap presentation

Heatmaps were created using the LRP method with $\alpha=1.0$ and $\beta=0.0$, as described in [2]. Each voxel is attributed a relevance score (R). To analyze relevance heatmaps, we qualitatively examined individual maps and calculated mean heatmaps for each configuration. For each mean heatmap, we generated a histogram of relevance values. Starting from the bin with the highest relevance, bin contents were iteratively summed until 40% of the total relevance was included. The lower bound of the final bin was used as the lower threshold for windowing the mean heatmap. All heatmaps presented in this study are overlaid on the MNI152 1 mm template and windowed to display the top 40% of relevance.

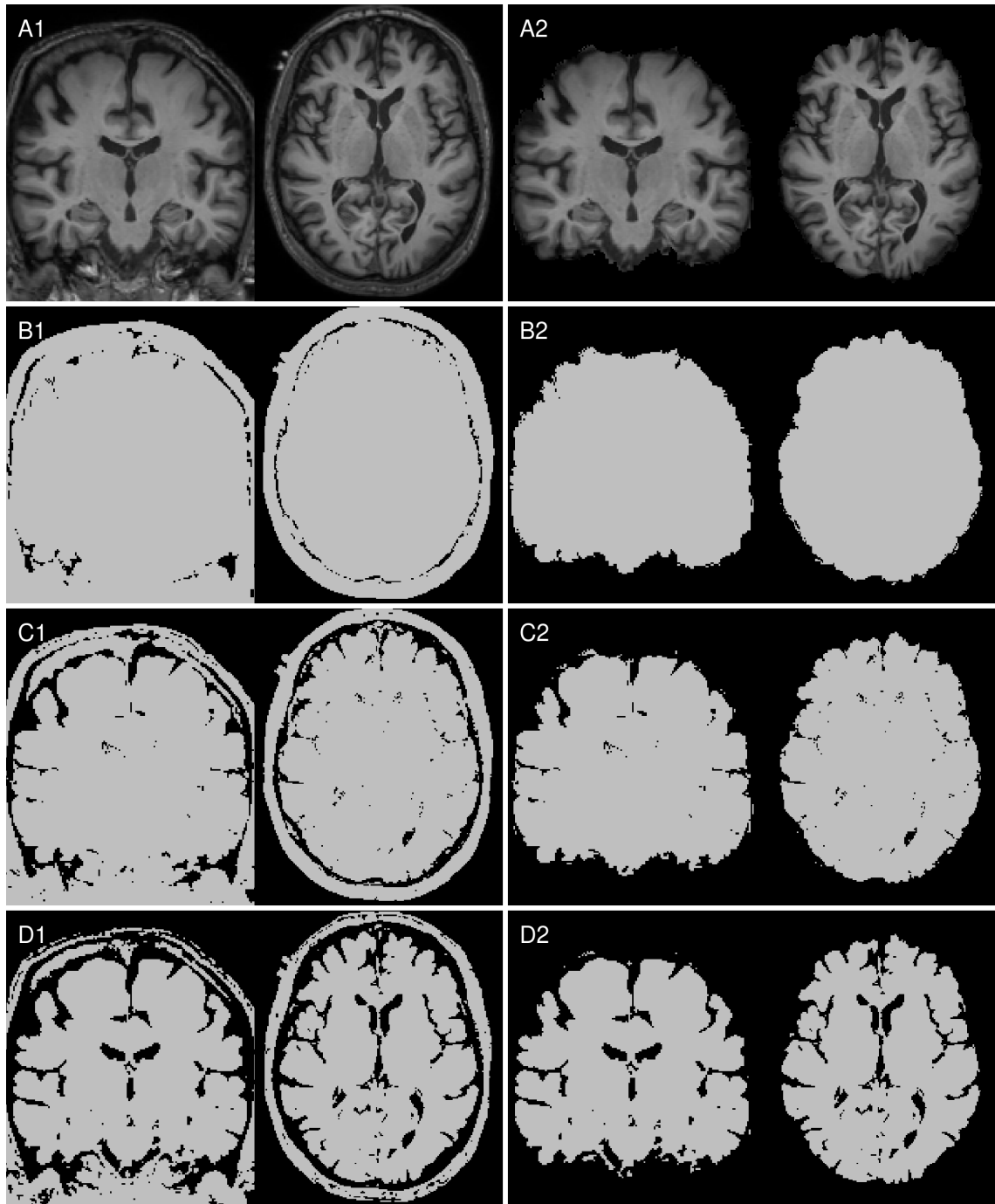


Fig. 1: Input image setups: Left column with (A1) aligned T1w MRI, identical binarized T1w images with the manually selected threshold levels (B1) 13.75%, (C1) 27.50% (C1) and (D1) 41.25%, and in the right column the corresponding skull-stripped versions (A2, B2, C2, D2).

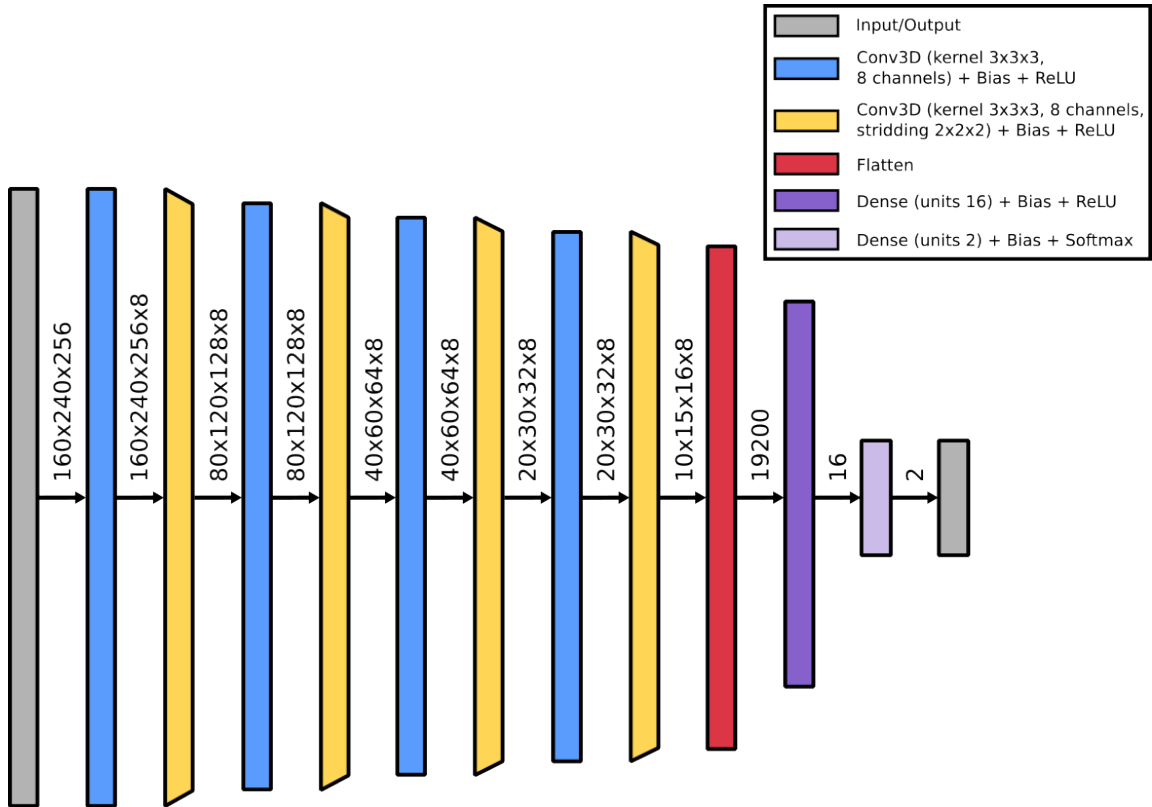


Fig. 2: Structure of the 3D classifier network. Dimensionalities between layers are the tensor sizes.

2.7 Random sampling

For each data sampling (10 samplings) and each network weight initialization (3 initializations), we retrained the network, resulting in 30 training sessions for each input image configuration [6]. Non-converging training sessions were excluded from further analysis. From the remaining sessions, the best-performing run based on validation accuracy was selected to create the mean heatmaps.

2.8 Statistical analysis

We calculated performance metrics, including accuracy, sensitivity, specificity, and the area under the receiver operating characteristic (ROC) curve, for all model configurations. Results are reported as mean values, standard deviations, and 95% confidence intervals. The model trained on skull-stripped T1w images (see A2 in Figure 1) was designated as the reference model for statistical comparisons. Exact McNemar tests were performed to compare accuracy, sensitivity, and specificity between the reference model and each alternative model for each session run (combination of data sampling and weight initialization), provided both runs were available [9]. To account for multiple comparisons involving overlapping data splits, we applied the discrete Bonferroni-Holm correction [37].

2.9 Heatmap similarity analysis

To evaluate heatmap similarities, we compared the best-performing run of the reference model with the corresponding runs (same data sampling and weight initialization) of each alternative model using structural image similarity measures. Before comparison heatmaps were normalized to min-max. Voxel-wise similarity was assessed with the root mean square error (RMSE), while global trends and overall similarity were evaluated using the Pearson correlation coefficient. Both global and localized patterns were analyzed with the mean structural similarity index measure (MSSIM) and Earth Mover’s Distance (Wasserstein distance). Additionally, binarized heatmaps highlighting the top 40% and top 10% relevance values were compared using the Intersection over Union (IoU) metric.

3 Results

3.1 Model performances

Table 2 provides the results of the accuracy, sensitivity, specificity, and AUC for all configurations in the random sampling setup. Performance metrics were evaluated across non-excluded training sessions for each model configuration. See Figure 4 and Figure 5 in Supplemental Material 2 for the analysis of misclassified samples and the corresponding heatmaps of models A2 and C2 with spectral clustering [21] and t-distributed stochastic neighbor embedding (t-SNE) [22] similar to the process described in [19].

Using an alpha level of .05 and discrete Bonferroni-Holm correction for multiple exact McNemar tests, comparisons between the reference model (skull-stripped, no binarization) and alternative configurations -including binarized skull-stripped images at thresholds of 13.75% (B2, 8 significant differences), 27.50% (C2, 1 significant difference), and 41.25% (D2, 4 significant differences) as well

as aligned images binarized at 41.25% (D1, 7 significant differences)- revealed little to no evidence for significant differences in accuracy, sensitivity, and specificity. 120 of 600 total comparisons remained significant after correction for multiple testing. See Table 6 in Supplemental Material for significant differences in model comparisons.

Aligned images with binarization thresholds 13.75% and 27.50% (B1, C1) performed comparably to aligned T1w images without binarization (A1). Similarly, skull-stripped images with binarization (B2, C2, D2) and aligned images binarized at 41.25% (D1) exhibited comparable performance to skull-stripped images without binarization (A2) while outperforming other aligned image configurations.

Table 2: Summary of performance metrics of all configurations. Note. AUC = area under receiver operating characteristics curve. Values between [and] show the 95% confidence interval.

Input images	Id	Binarizer	Accuracy	Sensitivity	Specificity	AUC
Aligned T1w	A1	None	71.12±5.01% [61.34%, 82.52%]	67.47±9.90% [51.66%, 85.94%]	74.76±7.07% [62.03%, 85.45%]	0.71±0.05 [0.62, 0.83]
	B1	13.75%	62.51±5.45% [53.39%, 72.09%]	62.26±9.48% [47.70%, 84.93%]	62.79±8.35% [46.56%, 74.42%]	0.63±0.054 [0.53, 0.72]
	C1	27.50%	72.74±5.49% [61.41%, 82.11%]	71.37±9.10% [56.86%, 88.87%]	74.15±9.94% [51.67%, 88.37%]	0.73±0.055 [0.61, 0.82]
	D1	41.25%	77.95±4.57% [70.90%, 86.34%]	76.74±9.41% [60.10%, 94.56%]	79.15±6.80% [64.54%, 89.56%]	0.78±0.045 [0.71, 0.86]
Skull-stripped T1w	A2	None	81.63±3.77% [74.36%, 88.01%]	81.22±6.94% [69.59%, 93.15%]	82.11±7.92% [65.50%, 93.60%]	0.82±0.037 [0.74, 0.88]
	B2	13.75%	78.12±4.63% [70.79%, 85.79%]	76.83±7.03% [62.65%, 87.05%]	79.40±6.76% [65.53%, 89.91%]	0.78±0.046 [0.71, 0.86]
	C2	27.50%	79.57±3.92% [73.46%, 86.45%]	78.32±7.74% [66.79%, 93.87%]	80.92±7.71% [67.53%, 91.95%]	0.80±0.039 [0.74, 0.86]
	D2	41.25%	81.56±4.63% [72.31%, 88.67%]	79.69±9.42% [62.59%, 96.48%]	83.50±6.77% [72.48%, 96.29%]	0.82±0.046 [0.72, 0.89]

3.2 Feature similarities

Figure 3 shows mean heatmaps for classification decisions on test images. Skull stripping enhances classification accuracy, while mean heatmaps from binarized inputs closely resemble those from non-binarized inputs.

Heatmaps from the skull-stripped model (A2) serve as the reference for structural heatmap comparisons in Table 3. Skull-stripped binarization (B2, C2, D2) shows lower voxel-wise dissimilarity (RMSE), higher global similarity (Pearson Correlation), and improved localized similarity (MSSIM, EMD) compared to the aligned versions (A1, B1, C1, D1). Among the binarized models, skull-stripped-binarization-13.75% (B2) demonstrates the highest overall structural similarity (RMSE, Pearson Correlation, MSSIM, EMD) with the reference (A2), while skull-stripped-binarization-27.50% exhibits the strongest regional overlap with the reference. These results emphasize the dominant role of volumetric features over T1w contrast variations.

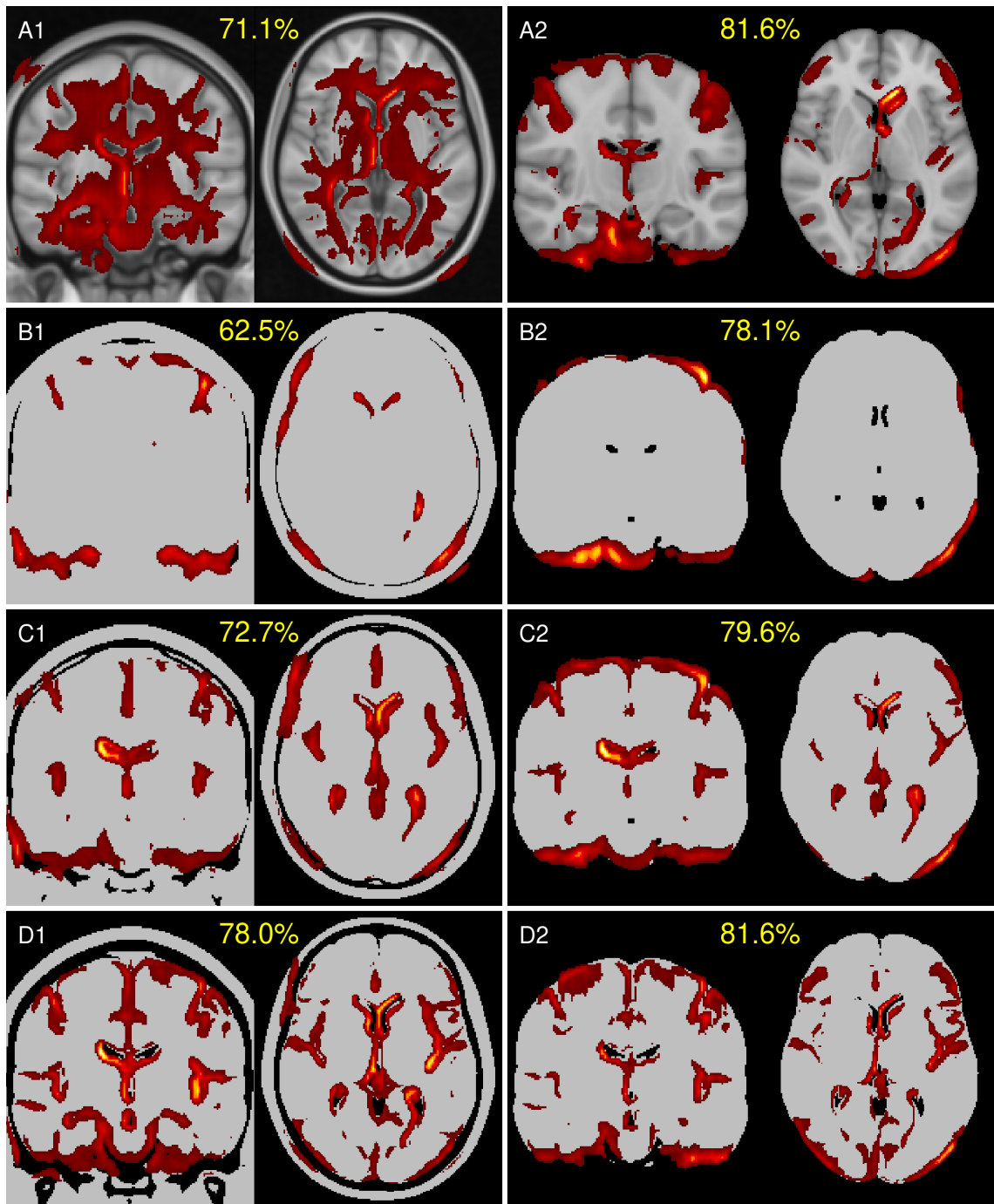


Fig. 3: Mean heatmaps from test images: Left column with (A1) aligned T1w MRI, identical binarized T1w image with threshold levels (B1) 13.75%, (C1) 27.50% (C1) and (D1) 41.25%, and right column with corresponding skull-stripped versions (A2, B2, C2, D2). The mean accuracies of the models are shown in yellow.

Table 3: Summary of heatmap similarity metrics for all configurations compared to the reference model (A2). Note. Values between [and] show the 95% confidence interval. Bin. = Binarizer, RMSE = root mean square error, Corr. = Correlation, MSSIM = mean structural similarity index measure, EMD = Earth Mover’s Distance, IoU = Intersection over Union, R = Relevance.

Input images	Id	Bin. %	RMSE	Pearson Corr.	MSSIM	EMD	IoU Top 40% R	IoU Top 10% R
Aligned T1w	A1	None	10.78±3.76 [5.98, 21.47]	0.13±0.04 [0.06, 0.21]	0.25±0.08 [0.12, 0.42]	8.44±3.25 [3.99, 17.48]	0.06±0.02 [0.02, 0.11]	0.01±0.01 [0.00, 0.03]
	B1	13.75	3.85±0.87 [2.25, 5.48]	0.08±0.03 [0.03, 0.15]	0.87±0.04 [0.78, 0.94]	0.50±0.29 [0.14, 1.29]	0.02±0.01 [0.01, 0.04]	0.00±0.00 [0.00, 0.01]
	C1	27.50	4.77±0.96 [3.07, 6.64]	0.18±0.05 [0.08, 0.26]	0.83±0.04 [0.74, 0.89]	0.71±0.45 [0.11, 1.71]	0.07±0.02 [0.03, 0.10]	0.01±0.01 [0.00, 0.02]
	D1	41.25	6.17±1.15 [3.98, 8.34]	0.23±0.05 [0.13, 0.30]	0.72±0.06 [0.62, 0.83]	1.61±0.62 [0.54, 2.75]	0.10±0.02 [0.05, 0.14]	0.01±0.01 [0.00, 0.03]
Skull- stripped T1w	A2	None	0.00±0.00	1.00±0.00	1.00±0.00	0.00±0.00	1.00±0.00	1.00±0.00
	B2	13.75	2.79±0.49 [1.97, 3.79]	0.58±0.07 [0.44, 0.69]	0.91±0.03 [0.82, 0.96]	0.39±0.25 [0.12, 1.05]	0.24±0.06 [0.13, 0.35]	0.15±0.03 [0.08, 0.21]
	C2	27.50	3.54±0.61 [2.45, 4.85]	0.56±0.07 [0.39, 0.67]	0.86±0.04 [0.78, 0.92]	0.73±0.44 [0.13, 1.67]	0.31±0.05 [0.20, 0.37]	0.17±0.03 [0.10, 0.24]
	D2	41.25	3.72±0.59 [2.69, 4.96]	0.51±0.08 [0.33, 0.65]	0.80±0.05 [0.68, 0.89]	1.01±0.50 [0.23, 2.12]	0.26±0.03 [0.18, 0.31]	0.16±0.04 [0.09, 0.22]

4 Discussion

Previous studies using T1w MRIs [33,4,20] have struggled to definitively identify the most relevant features -either volumetric changes, signal intensity variations, or other characteristics- underlying CNN-based classification of AD. Here, leveraging a large and representative AD dataset comprising 1,980 MR images from ADNI, we sought to disentangle these contributing factors by systematically eliminating T1w texture effects through binarization at varying threshold levels.

4.1 Study design and motivation

To ensure a robust and unbiased evaluation, we meticulously curated our dataset to include images with high inter-class image property similarity, reducing the risk of classification biases introduced by skewed class proportions [36]. Following this selection, we employed one-to-one matching based on sex and age to further mitigate potential covariate-driven influences on learned features. This stringent data construction aimed to minimize unwanted confounders, enabling the model to rely predominantly on structural changes and AD-related gray-white contrast alterations [7,27].

For all models non-linear registration is employed to align MR images to a standardized anatomical space (MNI152 template), aiming to account for inter-individual variations in brain morphology and native image resolutions. However, this approach does not fully compensate for the effects of atrophy, particularly in conditions like AD where tissue loss is spatially heterogeneous and disproportionately affects specific regions, such as the hippocampus and cortical gray matter. The effects of registration methods on classification performance and feature extraction have been explored in [33].

Skull-stripping, frequently employed in deep learning-driven AD classification, served as our reference model. This preprocessing step is motivated by prior studies incorporating heatmap explanations that achieved highest accuracies when applied in AD classification [4], dementia classification [20], multiple sclerosis classification [12] or in related tasks, such as brain age estimation [14,15,10].

Heatmaps generated in this study corroborate these findings, with relevance predominantly concentrated at the tissue boundary. To further probe the contribution of volumetric features, we removed tissue contrast entirely through binarization, isolating atrophic and structural features for analysis.

4.2 Binarization as a proxy for volumetric and structural features

We investigated three binarization levels, each aligned with the white matter intensity peak of the image, as depicted in Figure 1. These levels, although chosen arbitrarily, retained differing proportions of anatomical structures, capturing distinct aspects of atrophy, including ventricular enlargement, hippocampal shrinking and cerebellum morphology. As CNNs seem to focus on high-contrast regions [12,23], these binarization levels allowed us to systematically dissect how different volumetric and structural features influenced model predictions.

4.3 Performance comparisons

Performance metrics, summarized in Table 2, reveal that removing gray-white matter contrast while retaining skull-stripping has little to no effect on model performance. Statistical analyses using exact McNemar tests, adjusted with discrete Bonferroni-Holm correction ($\alpha = .05$), revealed minimal evidence of significant differences in accuracy, sensitivity, and specificity across configurations when compared to the reference model. Specifically, skull-stripped and binarized models at thresholds of 13.75%, 27.50%, and 41.25%, as well as aligned images binarized at 41.25%, showed fewer than 10% of comparisons with significant differences. This suggests that volumetric information is sufficient for achieving high classification accuracy in CNN-based AD classification, with minimal contribution from gray-white texture variations.

4.4 Similarity analysis of heatmaps

Given the consistent model performances across configurations, we examined structural image similarities using similarity metrics applied on heatmaps, shown in Table 3. Surprisingly, the model trained with binarization at 13.75% (B2) -which retains the most tissue within the brain mask- exhibited the highest similarity to the reference model (A2) across global (RMSE, Pearson correlation) and localized (MSSIM, EMD) similarity metrics. This indicates that the key volumetric and morphological features driving classification are predominantly encoded in the brain mask’s volume and shape.

Furthermore, starting at binarization-27.50% (C1, C2), models began to incorporate additional regions such as the ventricles, with binarization at 41.25% (D1, D2) capturing also hippocampal features. Notably, the highest overlaps between reference and binarized models were observed at 27.50% (C2), as indicated by intersection-over-union metrics. This suggests that contrast in ventricular regions in the reference model provides sufficient signal for the model to identify disease-relevant patterns.

Overall is the classification performance of the models driven by high contrast variations, either given by brain structures like the ventricular system and the hippocampi, or by being introduced artificially through image preprocessing.

4.5 Insights into preprocessing effects

Drawing parallels with the story of Mr. Pfungst and Clever Hans, where subtle cues in the experimental setup were inadvertently learned, we identified analogous issues in deep learning-based AD classification. Specifically, our findings reveal how preprocessing steps, foremost T1w skull-stripping, can inadvertently influence the model’s focus, emphasizing the need for careful control of preprocessing artifacts [33] and potentially the usage of quantitative MRI parameter maps [32].

4.6 Limitations

This study has its limitations. First, while the dataset is large, representative, and carefully crafted, it is derived from the ADNI database. However, the consistency and quality of ADNI data suggest that the findings should be generalizable to other cohorts and clinical settings. Second, our analysis primarily examines T1w images, preprocessing strategies, their impact on classification performance, and the features extracted using heatmaps. Third, the CNN architecture was optimized for the reference model (skull-stripped, no binarization) by systematically reducing trainable parameters and complexity, alongside hyperparameter tuning. Although the final architecture achieved performance metrics comparable to existing literature, applying the same setup across experiments aimed to minimize bias but may not eliminate it entirely. Lastly, while heatmaps and similarity metrics were effective for feature interpretation, they may not fully capture the intricate interactions between features learned by the models.

5 Conclusion

Our findings uncover a Clever Hans effect in deep learning-driven AD classification, demonstrating that models predominantly rely on volumetric features rather than microstructural changes in gray- and white matter. This highlights the critical need to evaluate data selection and preprocessing workflows to distinguish between artifacts and true disease-specific patterns, ensuring clinical relevance.

The implications of this work extend beyond AD classification, urging to adopt robust strategies for disentangling artifacts from meaningful features in deep learning workflows. Future studies should incorporate quantitative MRI parameters, such as T1, R2*, or QSM, to provide insights into disease pathology and enhance model interpretability and generalizability. By addressing these challenges, the field can advance toward more reliable and clinically actionable applications of AI in neuroimaging.

Data and code availability The code and the image ids (ADNI images) used in this study are available under <https://github.com/christiantinauer/binADNI>.

Acknowledgments. This study was funded by the Austrian Science Fund (FWF grant numbers: P30134, P35887). This research was supported by NVIDIA GPU hardware grants.

We thank Lukas Pirpamer for the feedback provided during the creation of this manuscript.

Data collection and sharing for the Alzheimer’s Disease Neuroimaging Initiative (ADNI) is funded by the National Institute on Aging (National Institutes of Health Grant U19AG024904). The grantee organization is the Northern California Institute for Research and Education. In the past, ADNI has also received funding from the National Institute of Biomedical Imaging and Bioengineering, the Canadian Institutes of Health Research, and private sector contributions through the Foundation for the National Institutes of Health (FNIH) including generous contributions from the following: AbbVie, Alzheimer’s Association; Alzheimer’s Drug Discovery Foundation; Araclon Biotech; BioClinica, Inc.; Biogen; Bristol-Myers Squibb Company; CereSpir, Inc.; Cogstate; Eisai Inc.; Elan Pharmaceuticals, Inc.; Eli Lilly and Company; EuroImmun; F. Hoffmann-La Roche Ltd and its affiliated company Genentech, Inc.; Fujirebio; GE Healthcare; IXICO Ltd.; Janssen Alzheimer Immunotherapy Research & Development, LLC.; Johnson & Johnson Pharmaceutical Research & Development LLC.; Lumosity; Lundbeck; Merck & Co., Inc.; Meso Scale Diagnostics, LLC.; NeuroRx Research; Neurotrack Technologies; Novartis Pharmaceuticals Corporation; Pfizer Inc.; Piramal Imaging; Servier; Takeda Pharmaceutical Company; and Transition Therapeutics.

Disclosure of Interests. The authors have no competing interests to declare that are relevant to the content of this article.

References

1. 2024 Alzheimer’s disease facts and figures. *Alzheimer’s & Dementia: The Journal of the Alzheimer’s Association* **20**(5), 3708–3821 (May 2024). <https://doi.org/10.1002/alz.13809>
2. Bach, S., Binder, A., Montavon, G., Klauschen, F., Müller, K.R., Samek, W.: On Pixel-Wise Explanations for Non-Linear Classifier Decisions by Layer-Wise Relevance Propagation. *PloS One* **10**(7), e0130140 (2015). <https://doi.org/10.1371/journal.pone.0130140>
3. Beach, T.G., Monsell, S.E., Phillips, L.E., Kukull, W.: Accuracy of the clinical diagnosis of Alzheimer disease at National Institute on Aging Alzheimer Disease Centers, 2005-2010. *Journal of Neuropathology and Experimental Neurology* **71**(4), 266–273 (Apr 2012). <https://doi.org/10.1097/NEN.0b013e31824b211b>
4. Böhle, M., Eitel, F., Weygandt, M., Ritter, K.: Layer-Wise Relevance Propagation for Explaining Deep Neural Network Decisions in MRI-Based Alzheimer’s Disease Classification. *Frontiers in Aging Neuroscience* **11**, 194 (2019). <https://doi.org/10.3389/fnagi.2019.00194>
5. Bouthillier, X., Delaunay, P., Bronzi, M., Trofimov, A., Nichyporuk, B., Szeto, J., Mohammadi Sepahvand, N., Raff, E., Madan, K., Voleti, V., Ebrahimi Kahou, S., Michalski, V., Arbel, T., Pal, C., Varoquaux, G., Vincent, P.: Accounting for Variance in Machine Learning Benchmarks. In: Smola, A., Dimakis, A., Stoica, I. (eds.) *Proceedings of Machine Learning and Systems*. vol. 3, pp. 747–769 (2021), https://proceedings.mlsys.org/paper_files/paper/2021/file/0184b0cd3cfb185989f858a1d9f5c1eb-Paper.pdf
6. Bradshaw, T.J., Huemann, Z., Hu, J., Rahmim, A.: A Guide to Cross-Validation for Artificial Intelligence in Medical Imaging. *Radiology. Artificial Intelligence* **5**(4), e220232 (Jul 2023). <https://doi.org/10.1148/ryai.220232>
7. Canu, E., McLaren, D.G., Fitzgerald, M.E., Bendlin, B.B., Zoccatelli, G., Alessandrini, F., Pizzini, F.B., Ricciardi, G.K., Beltramello, A., Johnson, S.C., Frisoni, G.B.: Mapping the structural brain changes in Alzheimer’s disease: The independent contribution of two imaging modalities. *Journal of Alzheimer’s Disease* **26**(Suppl 3), 263–274 (2011). <https://doi.org/10.3233/JAD-2011-0040>, <https://www.ncbi.nlm.nih.gov/pmc/articles/PMC3267543/>

8. Davatzikos, C.: Machine learning in neuroimaging: Progress and challenges. *NeuroImage* **197**, 652–656 (Aug 2019). <https://doi.org/10.1016/j.neuroimage.2018.10.003>
9. Dietterich, T.G.: Approximate Statistical Tests for Comparing Supervised Classification Learning Algorithms. *Neural Computation* **10**(7), 1895–1923 (Sep 1998). <https://doi.org/10.1162/089976698300017197>
10. Dinsdale, N.K., Bluemke, E., Smith, S.M., Arya, Z., Vidaurre, D., Jenkinson, M., Namburete, A.I.L.: Learning patterns of the ageing brain in MRI using deep convolutional networks. *NeuroImage* **224**, 117401 (Jan 2021). <https://doi.org/10.1016/j.neuroimage.2020.117401>
11. Dubois, B., Villain, N., Frisoni, G.B., Rabinovici, G.D., Sabbagh, M., Cappa, S., Bejanin, A., Bombois, S., Epelbaum, S., Teichmann, M., Habert, M.O., Nordberg, A., Blennow, K., Galasko, D., Stern, Y., Rowe, C.C., Salloway, S., Schneider, L.S., Cummings, J.L., Feldman, H.H.: Clinical diagnosis of Alzheimer’s disease: recommendations of the International Working Group. *The Lancet. Neurology* **20**(6), 484–496 (Jun 2021). [https://doi.org/10.1016/S1474-4422\(21\)00066-1](https://doi.org/10.1016/S1474-4422(21)00066-1)
12. Eitel, F., Soehler, E., Bellmann-Strobl, J., Brandt, A.U., Ruprecht, K., Giess, R.M., Kuchling, J., Asseyer, S., Weygandt, M., Haynes, J.D., Scheel, M., Paul, F., Ritter, K.: Uncovering convolutional neural network decisions for diagnosing multiple sclerosis on conventional MRI using layer-wise relevance propagation. *NeuroImage. Clinical* **24**, 102003 (2019). <https://doi.org/10.1016/j.nicl.2019.102003>
13. Henneman, W.J.P., Sluimer, J.D., Barnes, J., van der Flier, W.M., Sluimer, I.C., Fox, N.C., Scheltens, P., Vrenken, H., Barkhof, F.: Hippocampal atrophy rates in Alzheimer disease: added value over whole brain volume measures. *Neurology* **72**(11), 999–1007 (Mar 2009). <https://doi.org/10.1212/01.wnl.0000344568.09360.31>
14. Hofmann, S.M., Beyer, F., Lapuschkin, S., Goltermann, O., Loeffler, M., Müller, K.R., Villringer, A., Samek, W., Witte, A.V.: Towards the interpretability of deep learning models for multi-modal neuroimaging: Finding structural changes of the ageing brain. *NeuroImage* **261**, 119504 (Nov 2022). <https://doi.org/10.1016/j.neuroimage.2022.119504>
15. Hofmann, S.M., Goltermann, O., Scherf, N., Müller, K.R., Löffler, M., Villringer, A., Gaebler, M., Witte, A.V., Beyer, F.: The utility of explainable AI for MRI analysis: Relating model predictions to neuroimaging features of the aging brain. *Imaging Neuroscience* **3**, imag_a-00497 (Feb 2025). https://doi.org/10.1162/imag_a_00497, https://doi.org/10.1162/imag_a_00497
16. Jenkinson, M., Beckmann, C.F., Behrens, T.E.J., Woolrich, M.W., Smith, S.M.: FSL. *NeuroImage* **62**(2), 782–790 (Aug 2012). <https://doi.org/10.1016/j.neuroimage.2011.09.015>
17. Kingma, D.P., Ba, J.: Adam: A Method for Stochastic Optimization. In: Bengio, Y., LeCun, Y. (eds.) 3rd International Conference on Learning Representations, ICLR 2015, San Diego, CA, USA, May 7-9, 2015, Conference Track Proceedings (2015), <http://arxiv.org/abs/1412.6980>
18. Kline, A., Luo, Y.: PsmPy: A Package for Retrospective Cohort Matching in Python. Annual International Conference of the IEEE Engineering in Medicine and Biology Society. *IEEE Engineering in Medicine and Biology Society. Annual International Conference* **2022**, 1354–1357 (Jul 2022). <https://doi.org/10.1109/EMBC48229.2022.9871333>
19. Lapuschkin, S., Wäldchen, S., Binder, A., Montavon, G., Samek, W., Müller, K.R.: Unmasking Clever Hans predictors and assessing what machines really learn. *Nature Communications* **10**(1), 1096 (Mar 2019). <https://doi.org/10.1038/s41467-019-08987-4>
20. Leonardsen, E.H., Persson, K., Grødem, E., Dinsdale, N., Schellhorn, T., Roe, J.M., Vidal-Piñeiro, D., Sørensen, Ø., Kaufmann, T., Westman, E., Marquand, A., Selbæk, G., Andreassen, O.A., Wolfers, T., Westlye, L.T., Wang, Y.: Constructing personalized characterizations of structural brain aberrations in patients with dementia using explainable artificial intelligence. *NPJ digital medicine* **7**(1), 110 (May 2024). <https://doi.org/10.1038/s41746-024-01123-7>
21. von Luxburg, U.: A tutorial on spectral clustering. *Statistics and Computing* **17**(4), 395–416 (Dec 2007). <https://doi.org/10.1007/s11222-007-9033-z>, <https://doi.org/10.1007/s11222-007-9033-z>
22. Maaten, L.v.d., Hinton, G.: Visualizing Data using t-SNE. *Journal of Machine Learning Research* **9**(86), 2579–2605 (2008), <http://jmlr.org/papers/v9/vandermaaten08a.html>

23. Mattia, G.M., Villain, E., Nemmi, F., Le Lann, M.V., Franceries, X., Péran, P.: Investigating the discrimination ability of 3D convolutional neural networks applied to altered brain MRI parametric maps. *Artificial Intelligence in Medicine* **153**, 102897 (Jul 2024). <https://doi.org/10.1016/j.artmed.2024.102897>
24. Montavon, G., Samek, W., Müller, K.R.: Methods for interpreting and understanding deep neural networks. *Digital Signal Processing* **73**, 1–15 (Feb 2018). <https://doi.org/10.1016/j.dsp.2017.10.011>, <https://www.sciencedirect.com/science/article/pii/S1051200417302385>
25. Pfungst, O.: *Clever Hans (The Horse of Mr. Von Osten): A contribution to experimental animal and human psychology* (Oct 2010), <https://www.gutenberg.org/ebooks/33936>
26. Scheltens, P., De Strooper, B., Kivipelto, M., Holstege, H., Chételat, G., Teunissen, C.E., Cummings, J., van der Flier, W.M.: Alzheimer's disease. *The Lancet* **397**(10284), 1577–1590 (Apr 2021). [https://doi.org/10.1016/S0140-6736\(20\)32205-4](https://doi.org/10.1016/S0140-6736(20)32205-4), <https://www.sciencedirect.com/science/article/pii/S0140673620322054>
27. Serra, L., Cercignani, M., Lenzi, D., Perri, R., Fadda, L., Caltagirone, C., Macaluso, E., Bozzali, M.: Grey and white matter changes at different stages of Alzheimer's disease. *Journal of Alzheimer's disease: JAD* **19**(1), 147–159 (2010). <https://doi.org/10.3233/JAD-2010-1223>
28. Simonyan, K., Vedaldi, A., Zisserman, A.: Deep Inside Convolutional Networks: Visualising Image Classification Models and Saliency Maps. In: Bengio, Y., LeCun, Y. (eds.) 2nd International Conference on Learning Representations, ICLR 2014, Banff, AB, Canada, April 14-16, 2014, Workshop Track Proceedings (2014), <http://arxiv.org/abs/1312.6034>
29. Sluimer, J.D., Vrenken, H., Blankenstein, M.A., Fox, N.C., Scheltens, P., Barkhof, F., van der Flier, W.M.: Whole-brain atrophy rate in Alzheimer disease: identifying fast progressors. *Neurology* **70**(19 Pt 2), 1836–1841 (May 2008). <https://doi.org/10.1212/01.wnl.0000311446.61861.e3>
30. Smith, S.M., Zhang, Y., Jenkinson, M., Chen, J., Matthews, P.M., Federico, A., De Stefano, N.: Accurate, robust, and automated longitudinal and cross-sectional brain change analysis. *NeuroImage* **17**(1), 479–489 (Sep 2002). <https://doi.org/10.1006/ning.2002.1040>
31. Springenberg, J.T., Dosovitskiy, A., Brox, T., Riedmiller, M.A.: Striving for Simplicity: The All Convolutional Net. In: Bengio, Y., LeCun, Y. (eds.) 3rd International Conference on Learning Representations, ICLR 2015, San Diego, CA, USA, May 7-9, 2015, Workshop Track Proceedings (2015), <http://arxiv.org/abs/1412.6806>
32. Tinauer, C., Damulina, A., Sackl, M., Soellradl, M., Achtibat, R., Dreyer, M., Pahde, F., Lapuschkin, S., Schmidt, R., Ropele, S., Samek, W., Langkammer, C.: Explainable Concept Mappings of MRI: Revealing the Mechanisms Underlying Deep Learning-Based Brain Disease Classification. In: Longo, L., Lapuschkin, S., Seifert, C. (eds.) *Explainable Artificial Intelligence*. pp. 202–216. Springer Nature Switzerland, Cham (2024). https://doi.org/10.1007/978-3-031-63797-1_11
33. Tinauer, C., Heber, S., Pirpamer, L., Damulina, A., Schmidt, R., Stollberger, R., Ropele, S., Langkammer, C.: Interpretable brain disease classification and relevance-guided deep learning. *Scientific Reports* **12**(1), 20254 (Nov 2022). <https://doi.org/10.1038/s41598-022-24541-7>
34. Tustison, N.J., Avants, B.B., Cook, P.A., Zheng, Y., Egan, A., Yushkevich, P.A., Gee, J.C.: N4ITK: improved N3 bias correction. *IEEE transactions on medical imaging* **29**(6), 1310–1320 (Jun 2010). <https://doi.org/10.1109/TMI.2010.2046908>
35. Wallis, D., Buvat, I.: Clever Hans effect found in a widely used brain tumour MRI dataset. *Medical Image Analysis* **77**, 102368 (Apr 2022). <https://doi.org/10.1016/j.media.2022.102368>
36. Wen, J., Thibeau-Sutre, E., Diaz-Melo, M., Samper-González, J., Routier, A., Bottani, S., Dormont, D., Durrleman, S., Burgos, N., Colliot, O., Alzheimer's Disease Neuroimaging Initiative, Australian Imaging Biomarkers and Lifestyle flagship study of ageing: Convolutional neural networks for classification of Alzheimer's disease: Overview and reproducible evaluation. *Medical Image Analysis* **63**, 101694 (Jul 2020). <https://doi.org/10.1016/j.media.2020.101694>
37. Westfall, P.H., Troendle, J.F., Pennello, G.: Multiple McNemar tests. *Biometrics* **66**(4), 1185–1191 (Dec 2010). <https://doi.org/10.1111/j.1541-0420.2010.01408.x>

Supplemental Material 1

Table 4 shows the distribution of the preselected images across sites, vendors and research groups, while Table 5 displays the distribution of the same images across vendors, imaging protocols and research groups.

Table 4: Distribution of preselected images across sites, vendors and research groups.

Phase	ADNI 2
Field Strength	3.0 tesla
Acquisition Plane	SAGITTAL
Pixel Spacing X	- multiple -
Pixel Spacing Y	- multiple -
Weighting	T1
Slice Thickness	1.2 mm

Count - Image Id		Research Group		Total Result
Site ID	Manufacturer	AD	CN	
002	Philips Medical Systems	8	84	92
003	GE MEDICAL SYSTEMS	36	78	114
005	GE MEDICAL SYSTEMS	31	3	34
006	Philips Medical Systems	34	52	86
007	GE MEDICAL SYSTEMS	22	60	82
009	SIEMENS	23	44	67
010	Philips Medical Systems	2	20	22
011	SIEMENS	36	75	111
012	Philips Medical Systems		36	36
013	Philips Medical Systems	6	26	32
	SIEMENS	4	12	16
014	SIEMENS	18	46	64
016	GE MEDICAL SYSTEMS	50	52	102
	SIEMENS		2	2
018	Philips Medical Systems	18	54	72
019	Philips Medical Systems	45	24	69
021	GE MEDICAL SYSTEMS	10	55	65
022	SIEMENS		56	56
023	SIEMENS	16	38	54
024	SIEMENS	34	24	58
027	GE MEDICAL SYSTEMS	40		40
029	GE MEDICAL SYSTEMS	8	69	77
031	Philips Medical Systems	8	48	56
032	SIEMENS	8	48	56
033	SIEMENS	24	56	80
035	SIEMENS	6	29	35
036	SIEMENS	34	32	66
	SIEMENS PixelMed	2	2	4
037	SIEMENS	31	65	96
041	SIEMENS		80	80
051	SIEMENS	15		15
052	GE MEDICAL SYSTEMS	16		16
053	Philips Medical Systems	10	12	22
057	GE MEDICAL SYSTEMS		4	4
	SIEMENS	2		2
067	SIEMENS	12	12	24
068	SIEMENS	10	28	38
070	SIEMENS	6	20	26

072	SIEMENS		18	18
073	SIEMENS	11	122	133
082	SIEMENS	9	48	57
094	GE MEDICAL SYSTEMS	21	52	73
098	GE MEDICAL SYSTEMS	16	56	72
099	GE MEDICAL SYSTEMS		12	12
	SIEMENS	6	24	30
100	Philips Medical Systems	2	24	26
109	GE MEDICAL SYSTEMS	2	10	12
114	SIEMENS	9	5	14
116	SIEMENS	43	70	113
123	SIEMENS	10	2	12
126	GE MEDICAL SYSTEMS	18		18
127	GE MEDICAL SYSTEMS	69	58	127
128	SIEMENS	20	52	72
129	GE MEDICAL SYSTEMS		38	38
	Philips Healthcare		16	16
130	Philips Medical Systems	83	24	107
131	GE MEDICAL SYSTEMS		8	8
	Philips Healthcare	4		4
135	SIEMENS	44	34	78
136	Philips Medical Systems	2	20	22
137	SIEMENS	38	72	110
141	SIEMENS		2	2
153	SIEMENS	10	38	48
941	SIEMENS		76	76
Total Result		1042	2227	3269

Table 5: Distribution of preselected images across vendors, imaging protocols and research groups.

Phase	ADNI 2
Acquisition Plane	SAGITTAL
Field Strength	3.0 tesla
Pixel Spacing X	- multiple -
Pixel Spacing Y	- multiple -
Weighting	T1
Slice Thickness	1.2 mm

Count - Image Id		Research Group		
Manufacturer	Description	AD	CN	Total Result
GE MEDICAL SYSTEMS	Accelerated Sag IR-FSPGR	59	55	114
	Accelerated Sag IR-SPGR	105	191	296
	Accelerated SAG IR-SPGR REPEAT		2	2
	IR-SPGR	3	28	31
	IR-SPGR w/acceleration	3	28	31
	Sag IR-FSPGR	59	57	116
	Sag IR-SPGR	109	194	303
	Sag IR-SPGR REPEAT	1		1
Philips Healthcare	MPRAGE	2	8	10
	MPRAGE SENSE2	2	8	10
Philips Medical Systems	MPRAGE	108	212	320
	MPRAGE SENSE		1	1
	MPRAGE SENSE2	110	210	320
	MPRAGE SENSE2 SENSE		1	1
SIEMENS	MPRAGE	233	579	812
	MPRAGE GRAPPA 2	1	3	4
	MPRAGE GRAPPA 2_ND	1	3	4
	MPRAGE GRAPPA2	181	487	668
	MPRAGE GRAPPA2_S3_DIS3D		2	2
	MPRAGE Repeat	1		1
	MPRAGE_NO ANGLE		2	2
	MPRAGE_NO ANGLE=		12	12
	MPRAGE_Sag - NO ANGLE=	2	3	5
	MPRAGE_GRAPPA2	48	84	132
	MPRAGE_ND	1	3	4
	MPRAGE_P2_NO ANGLE		2	2
	MPRAGE_P2_NO ANGLE=	2	15	17
	MPRAGE_S2_DIS2D		1	1
	MPRAGE_S2_DIS3D	1	16	17
	SAG MPRAGE GRAPPA2 NO ANGLE	4	9	13
	SAG MPRAGE NO ANGLE	4	9	13
	SIEMENS PixelMed	MPRAGE	1	1
MPRAGE_GRAPPA2		1	1	2
Total Result		1042	2227	3269

Supplemental Material 2

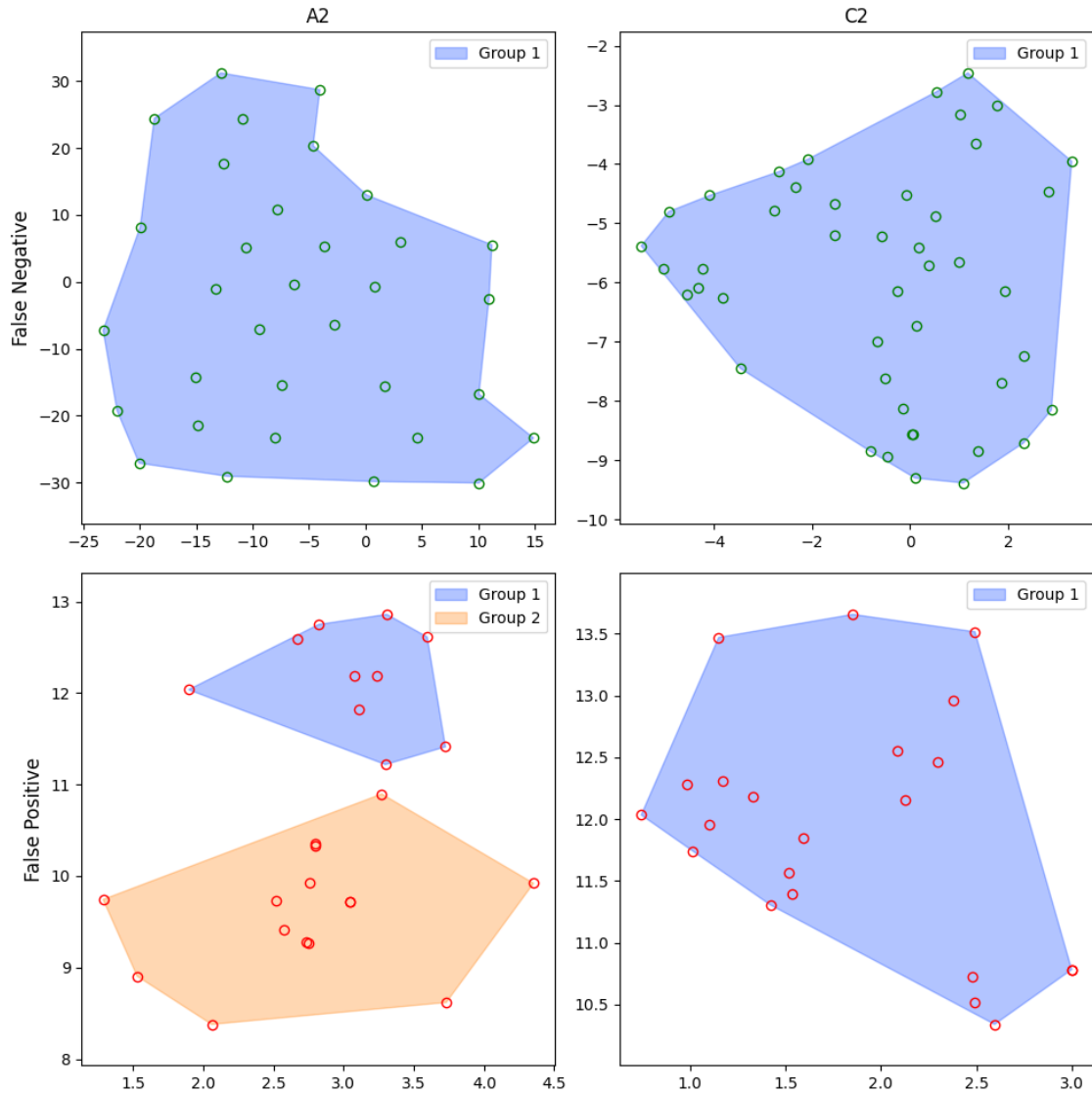


Fig. 4: t-SNE visualization of heatmaps for False Negative (row 1) and False Positive (row 2) classified samples for the reference model (A2) and the 27.5% binarization model (C2). Only the heatmaps for False Positive classified samples of model A2 exhibit 2 clusters, while all other heatmaps are grouped into 1 cluster.

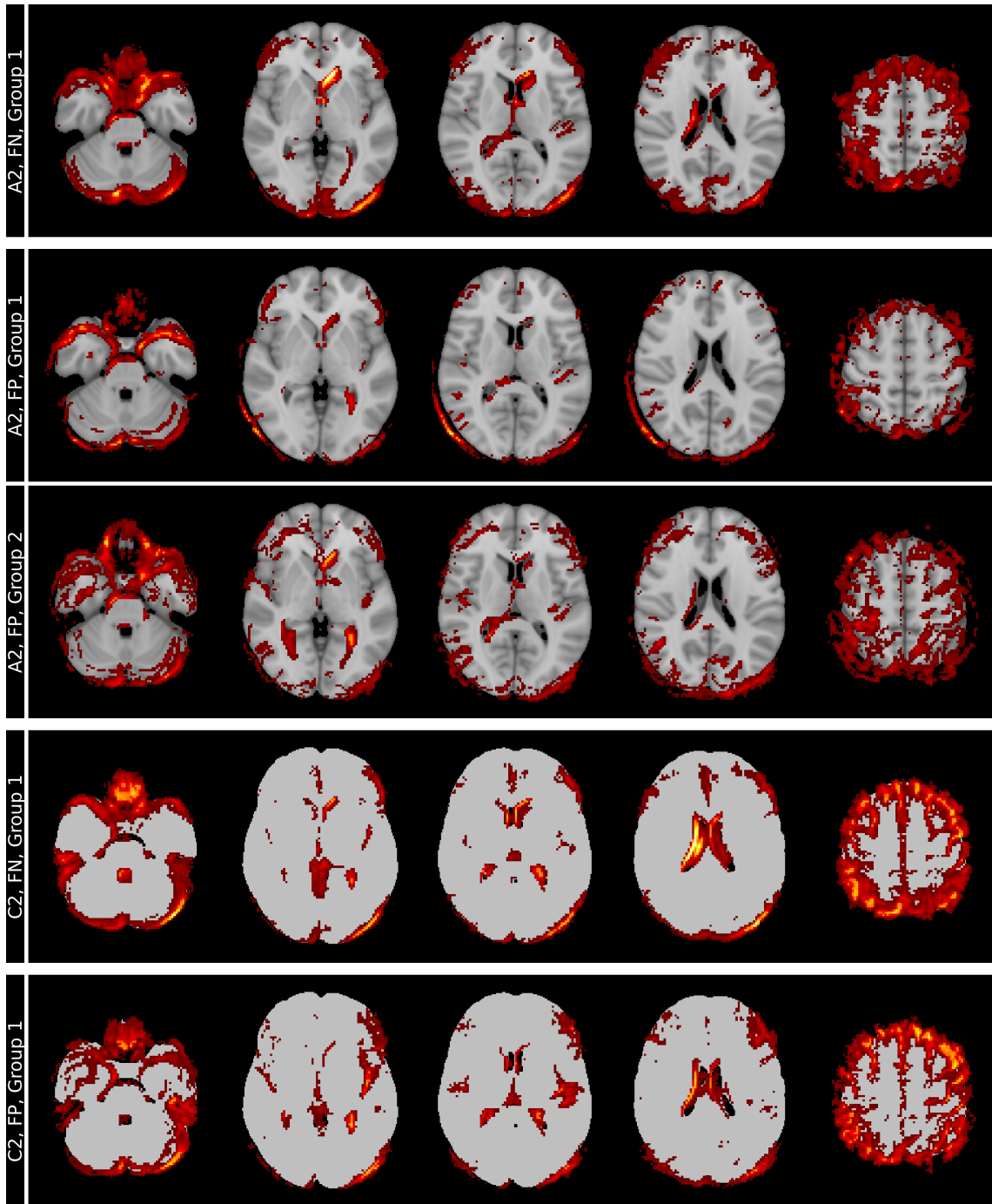


Fig. 5: Mean heatmaps for the groups identified using the individual heatmaps and spectral clustering for misclassifications of models A2 and C2. Model A2 (skull-stripping) shows a clear separation between False Negative (row 1, Group 1) and False Positive (row 2, Group 1) in the shape of the temporal lobe (column 1). In row 3 (A2, False Positive, Group 2) the ventricles are more pronounced (column 2) compared to heatmaps for False Negative analysis in row 1. Comparison of model C2 shows also differences in the temporal lobes, the ventricles and the cortex. Note. FN: False Negative, FP: False Positive.

Supplemental Material 3

Table 6: Multiple testing using two-sided p-values for multiple models and performance measures. Note. Comparison denotes models and measure; e.g., “A2-B1, acc” compares models A2 (skull-stripped, no-binarization) and B1 (binarized-13.75%) with respect to the overall accuracy. Θ_1 and Θ_2 refers to the respective performance metrics. Adj. p-value is the discrete Bonferroni-Holm corrected p-value of the comparison. The table shows only the 122 significant differences of the multiple testing and the first non-significant difference. Remaining results are indicated with “(477 more)”.

Comparison	Θ_1	Θ_2	Sampling Index	Initial Weights Index	Adj. p-value
A2-B1, acc	0.84	0.55	9	2	0.00000
A2-B1, acc	0.89	0.58	9	3	0.00000
A2-B1, acc	0.88	0.61	2	3	0.00000
A2-B1, acc	0.83	0.54	8	1	0.00000
A2-B1, spe	0.89	0.50	9	2	0.00000
A2-C1, spe	0.89	0.52	9	2	0.00000
A2-B1, acc	0.84	0.62	7	3	0.00000
A2-B1, acc	0.80	0.53	4	1	0.00000
A2-A1, acc	0.86	0.68	1	2	0.00000
A2-B1, spe	0.94	0.64	7	3	0.00000
A2-B1, acc	0.83	0.58	2	2	0.00000
A2-B1, acc	0.87	0.62	10	2	0.00000
A2-B1, acc	0.84	0.59	9	1	0.00000
A2-B1, acc	0.86	0.63	4	2	0.00000
A2-A1, sen	0.90	0.57	10	2	0.00000
A2-B1, sen	0.93	0.63	9	3	0.00000
A2-A1, sen	0.87	0.60	1	2	0.00000
A2-A1, spe	0.94	0.69	7	3	0.00000
A2-C1, acc	0.84	0.61	9	2	0.00000
A2-B1, sen	0.90	0.59	3	3	0.00000
A2-C1, spe	0.82	0.52	1	3	0.00000
A2-B1, acc	0.86	0.68	1	2	0.00000
A2-C1, acc	0.86	0.67	1	2	0.00000
A2-A1, acc	0.82	0.60	4	3	0.00000
A2-B1, acc	0.79	0.57	5	3	0.00000
A2-B1, spe	0.89	0.61	9	1	0.00000
A2-B1, acc	0.81	0.61	10	1	0.00000
A2-B1, sen	0.87	0.58	10	3	0.00000
A2-B1, sen	0.80	0.47	8	1	0.00000
A2-B1, sen	0.82	0.51	2	3	0.00000
A2-B1, sen	0.90	0.60	10	2	0.00001
A2-A1, acc	0.86	0.67	4	2	0.00001
A2-B2, acc	0.89	0.73	9	3	0.00001
A2-B1, acc	0.81	0.59	8	2	0.00001

A2-B1, spe	0.85	0.52	9	3	0.00001
A2-C1, acc	0.83	0.64	8	1	0.00001
A2-A1, acc	0.87	0.70	10	2	0.00001
A2-B1, spe	0.94	0.72	2	3	0.00001
A2-B1, spe	0.90	0.62	4	2	0.00001
A2-B1, acc	0.81	0.63	3	1	0.00002
A2-C1, acc	0.81	0.61	8	2	0.00002
A2-B1, acc	0.76	0.56	10	3	0.00003
A2-D2, spe	0.85	0.66	10	2	0.00003
A2-B1, spe	0.87	0.61	4	3	0.00004
A2-C1, sen	0.90	0.64	10	2	0.00004
A2-B2, spe	0.66	0.89	10	3	0.00006
A2-D1, sen	0.82	0.53	4	2	0.00006
A2-A1, acc	0.81	0.62	8	2	0.00007
A2-C1, sen	0.80	0.55	8	1	0.00008
A2-C1, acc	0.87	0.71	10	2	0.00008
A2-B1, acc	0.82	0.64	4	3	0.00008
A2-D1, acc	0.86	0.71	1	2	0.00009
A2-B1, spe	0.83	0.52	4	1	0.00009
A2-A1, spe	0.90	0.64	4	2	0.00011
A2-A1, sen	0.94	0.74	5	2	0.00013
A2-B1, spe	0.86	0.61	8	1	0.00014
A2-B1, acc	0.84	0.68	1	1	0.00015
A2-B1, sen	0.81	0.54	2	2	0.00024
A2-A1, acc	0.88	0.75	2	3	0.00025
A2-A1, sen	0.75	0.47	8	2	0.00025
A2-A1, acc	0.81	0.66	3	1	0.00028
A2-C1, acc	0.81	0.66	1	3	0.00031
A2-D1, spe	0.66	0.87	10	3	0.00032
A2-C1, sen	0.87	0.64	1	2	0.00034
A2-B1, sen	0.78	0.54	4	1	0.00039
A2-A1, spe	0.87	0.66	4	3	0.00042
A2-B1, acc	0.82	0.67	7	2	0.00052
A2-B1, spe	0.85	0.62	2	2	0.00065
A2-B1, spe	0.92	0.71	7	1	0.00105
A2-D1, sen	0.90	0.66	10	2	0.00104
A2-B1, spe	0.83	0.60	3	1	0.00108
A2-C1, acc	0.82	0.69	7	2	0.00162
A2-C1, acc	0.89	0.75	9	3	0.00161
A2-B2, sen	0.82	0.63	4	2	0.00224
A2-D2, acc	0.79	0.89	5	3	0.00224
A2-B1, sen	0.75	0.48	8	2	0.00235
A2-D2, sen	0.78	0.58	4	1	0.00278
A2-B2, acc	0.86	0.74	4	2	0.00281

A2-B1, acc	0.80	0.66	7	1	0.00285
A2-B2, spe	0.85	0.64	9	3	0.00289
A2-D2, spe	0.65	0.81	5	3	0.00294
A2-A1, spe	0.89	0.71	9	2	0.00385
A2-A1, acc	0.84	0.72	1	1	0.00471
A2-D1, acc	0.86	0.71	4	2	0.00612
A2-B1, spe	0.80	0.59	10	1	0.00760
A2-D1, sen	0.87	0.66	1	2	0.00759
A2-B1, sen	0.82	0.60	6	1	0.00776
A2-B2, spe	0.94	0.76	7	3	0.00774
A2-C1, spe	0.88	0.65	8	2	0.00779
A2-A1, sen	0.81	0.62	2	1	0.00786
A2-A1, acc	0.82	0.69	7	2	0.00822
A2-B1, spe	0.65	0.39	5	3	0.00861
A2-A1, acc	0.89	0.77	9	3	0.00975
A2-B2, sen	0.75	0.88	7	3	0.00985
A2-B1, sen	0.79	0.59	9	2	0.01137
A2-C1, sen	0.81	0.61	2	2	0.01135
A2-A1, sen	0.79	0.59	1	3	0.01203
A2-B1, spe	0.85	0.67	1	2	0.01280
A2-A1, acc	0.80	0.69	7	1	0.01469
A2-B1, spe	0.85	0.63	10	2	0.01656
A2-A1, acc	0.79	0.68	2	1	0.01664
A2-A1, spe	0.94	0.79	2	3	0.01694
A2-D1, spe	0.65	0.85	5	3	0.01915
A2-C1, sen	0.93	0.77	9	3	0.01916
A2-C1, acc	0.81	0.68	10	1	0.01927
A2-A1, spe	0.90	0.72	7	2	0.02008
A2-C1, sen	0.90	0.73	3	3	0.02038
A2-B1, sen	0.87	0.69	1	2	0.02084
A2-C1, acc	0.83	0.70	2	2	0.02126
A2-B1, sen	0.79	0.57	9	1	0.02497
A2-B1, spe	0.88	0.69	1	1	0.02553
A2-C1, acc	0.86	0.72	4	2	0.02597
A2-A1, acc	0.83	0.71	8	1	0.02820
A2-B2, spe	0.66	0.81	3	3	0.02896
A2-B1, spe	0.90	0.72	7	2	0.02998
A2-C2, spe	0.66	0.81	3	3	0.03210
A2-A1, sen	0.82	0.64	10	1	0.03369
A2-B1, sen	0.93	0.75	5	3	0.03393
A2-A1, acc	0.84	0.74	7	3	0.03642
A2-B1, acc	0.77	0.63	3	2	0.03756
A2-B1, acc	0.79	0.66	2	1	0.03768
A2-C1, acc	0.81	0.69	3	1	0.03935

A2-C1, spe	0.89	0.72	9	1	0.05069
(477 more)	⋮	⋮	⋮	⋮	⋮